Experimental Study for Nondestructive Evaluation of Embedded Tendons in Ground Anchors Using an Elasto-Magnetic Sensor: Verification Through Numerical Finite Element Simulations

Dongyoung Ko, Jooyoung Park, Junkyeong Kim, c, Hyungchul Yoon, and Seunghee Park

***Abstract*—Tendon damage is a major risk of prestressed structures. Ground anchors are structural elements that introduce high levels of prestress, typically over 1000 kN. Tendon damage can threaten the stability of the structure they support. Particularly, the visual inspection of buried ground anchor tendons is impossible. Thus, assessing tendon damage is essential during its service life. In this study, an embedded tendon damage detection method based on the magnetostriction effect is developed. A parametric study was conducted to optimize the sensor parameters through numerical simulations based on the finite element method (FEM). Based on the results, the elasto-magnetic (EM) sensor was fabricated. Different damage degrees in tendons were measured at room temperature using the fabricated EM sensor. Subsequently, the induced electromotive force (EMF) and magnetic flux density were obtained. The finite element simulation results showed a quadratic relationship between the effective cross-sectional area reduction ratio (ARR) of the specimen due to damage and the peak of magnetic flux density. The experimental results were compared with the simulation results. This study introduces a promising nondestructive evaluation (NDE) method for detecting damage in the embedded tendon of ground anchors and demonstrates a design methodology for EM sensors suitable for the target object.**

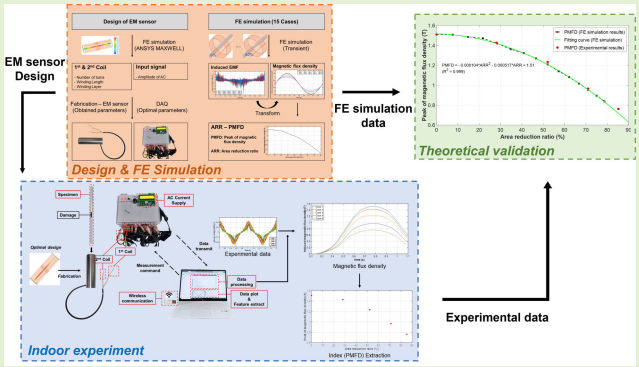

***Index Terms*—Elasto-magnetic (EM) sensor, finite element (FE) simulation, ground anchor, magnetostriction effect, tendon damage.**

I. Introduction

GROUND anchors are major construction elements widely used in civil engineering structures, such as bridges and dams, to resist tensile forces. They are typically installed to stabilize slopes and prevent landslides and rockfalls. Ground anchors are installed horizontally in the soil or rock and tensioned to hold the slope in place. In addition, they are often used to reinforce retaining walls and prevent them from collapsing under the weight of soil or water pressure. Over time, these anchors may deteriorate owing to factors, such as corrosion, fatigue, and overloading, which can compromise the structural integrity of the entire system. Damage can cause serious accidents because a high prestress is applied during construction. In particular, tendon damage can create several hazards that can lead to the collapse of retaining walls and structures. Ground anchor accidents can have catastrophic consequences, such as damage to civil engineering structures and property and loss of life [1], [2], [3].

Tendons can be damaged for several reasons. Corrosion can occur owing to moisture exposure, soil acidity, chloride concentration of the grout, or other environmental factors.

Manuscript received 3 September 2023; accepted 21 September 2023. Date of publication 2 October 2023; date of current version 31 October 2023. This work was supported in part by the Technology Development Program funded by the Ministry of SMEs and Startups (MSS, Korea), Korea Ministry of Land, Infrastructure and Transport (MOLIT) as Innovative Talent Education Program for Smart City under Grant S3174912; and in part by the National Research Foundation of Korea (NRF) Grant funded by the Korean Government (MSIT) under Grant NRF-2021R1A4A3033128; and in part by the "National Research and Development Project for Smart Construction Technology" under Grant 22SMIP-A158708-03 funded by the Korea Agency for Infrastructure Technology Advancement under the Ministry of Land, Infrastructure and Transport, and managed by the Korea Expressway Corporation. The associate editor coordinating the review of this article and approving it for publication was Prof. Qiliang Li. *(Corresponding author: Seunghee Park.)*

Please see the Acknowledgment section of this paper for the author affiliations.

Digital Object Identifier 10.1109/JSEN.2023.3319215

In particular, the local corrosion of ground anchor tendons can spread rapidly. The effective cross-sectional area of the tendon decreases as the degree of corrosion increases, weakening the entire anchor system. Moreover, this leads to a loss of tension in the anchor. Consequently, the anchor may lose its ability to sufficiently support the structures, causing instability. This can be dangerous if the retaining wall is in a densely populated area or near important infrastructure. A disastrous slope failure occurred on Freeway No.3 on April 25, 2010, in Northern Taiwan. The primary reason for the failure was that most anchors were severely corroded, and their steel strands were broken [4], [5]. This accident highlighted the crucial need to detect any damage to ground anchors at an early stage to prevent catastrophic failures. Moreover, unlike other structures in which tendons are exposed externally, visual inspection is impossible for embedded ground anchors. Therefore, it is crucial to develop a technique for inspecting the structural stability of embedded ground anchors during their service life.

Nondestructive evaluation (NDE) techniques are essential for assessing the conditions of embedded structures in civil engineering. NDE techniques can ensure the safety and reliability of these structures by providing an accurate method for detecting damage and assessing the conditions of the embedded structure [6], [7], [8] [9], [10], [11] [12], [13], [14]. Extensive research on NDE-based damage detection for several metallic materials in construction has been conducted over the last decades; however, few NDE techniques have been designed for assessing damage to embedded tendons. Zima and Rucka [15] proposed a damage assessment method based on wave propagation. A solution for selecting the excitation frequency was provided. In addition, the time interval was inversely proportional to the bonding length; however, tendon damage could not be quantified. No previous studies have assessed damage in ground anchor tendons. Some studies used NDE techniques, such as the magnetic flux leakage (MFL) [16], [17], [18], optical detection method [19], [20], [21], [22], ultrasonic guided wave (UGW) [23], [24], [25], and acoustic emission (AE) [26], [27], [28], [29] for estimating damage in embedded structures. However, these methods may not be suitable for assessing damage in embedded structural elements, including ground anchor tendons. MLF is a movable sensor, making it impossible to apply it to a buried structure. Furthermore, UGW, AE systems, and optical sensors require expensive equipment, making them unsuitable for application to ground anchors that require a large quantity installation on a single structure.

Using an elasto-magnetic (EM) sensor is an NDE technique for estimating the tension force in ground anchors. Its theoretical basis is widely known. An EM sensor measures the changes in magnetic fields induced by the mechanical stress or deformation of a metallic material [30]. It is highly sensitive to magnetic field changes, allowing it to detect even small physical changes in metallic structures. Moreover, it can be used to rapidly and efficiently inspect large areas of metallic structures, reducing the time and cost associated with traditional inspection methods. Furthermore, EM sensors are easy to manufacture, allowing them to be tailored to the shape of any test object. The tension force estimation technique for structural materials based on EM sensors has been in development for a long time, and its performance has been validated through numerous research up to the present day. In 1996, Kvasnica and Fabo [41] developed the instrumentation for magnetic measurement of mechanical stress in steel wires. They found that the changes in magnetic properties are very sensitive to the external tension variation in the steel wires. In 1999, Wang et al. [42] verified the cable stress monitoring performance of the magnetoelastic sensor on bridge. Since then, the number of research has been conducted to enhance the estimation of tensile force using EM sensor. Recently, there is a trend of applying machine learning to the data obtained through measurements using EM sensors, aiming to predict more accurate tensile force. In 2019, Kim and Park [7] proposed a machine learning-based tensile force estimation technique for prestressed concrete bridges using EM sensor. However, there are few studies focused on utilizing EM sensors for the purpose of damage detection.

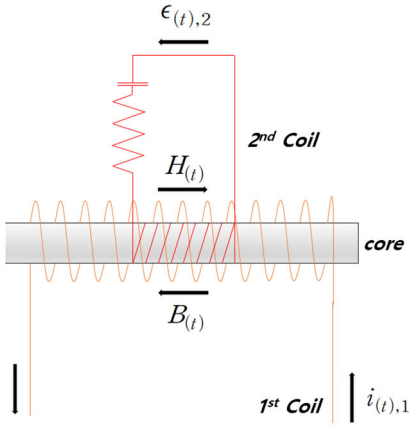

Fig. 1. Principle of EM sensor measurement.

This study demonstrates the possibility of detecting damage in ground anchors by using an EM sensor. A design process considering the electromagnetic characteristics of the materials and target object is essential for fabricating an EM sensor. However, several studies have not considered this. Therefore, in this study, the sensor parameters were initially determined through a finite element (FE) simulation, considering the size and form of an actual ground anchor. Subsequently, an indoor experiment was performed to verify the possibility of detecting tendon damage using a fabricated EM sensor by measuring the electromotive force (EMF). Finally, the experiment results were compared with the FE simulation results.

II. Theoretical Background

A. Principle of EM Sensor

In this study, the electromagnetic signal of a damaged steel rod was measured based on its effective cross-sectional area using an EM sensor. An understanding of electromagnetic induction is necessary to understand this principle. Fig. 1 illustrates the principle of EM sensor measurement [30], [31].

When an alternating current (ac) flows through the first coil, the material is magnetized, causing a potential difference in the material. Consequently, an induced EMF is generated in

the second coil. This phenomenon is known as electromagnetic induction. The induced potential difference is proportional to the rate of change in the magnetic flux over time and the number of turns in the coil. The EMF induced in the second coil can be expressed as follows [30]:

$$\epsilon_{(t),2} = -N_2 \frac{d\Phi_{(t)}}{dt} \tag{1}$$

where $\epsilon_{(t),2}$ denotes the induced EMF in the second coil, N_2 denotes the number of turns in the first coil, and $\Phi_{(t)}$ denotes the magnetic flux passing through the coil.

Magnetic flux density $B_{(t)}$ is generated when a magnetic material is subjected to a magnetizing force $H_{(t)}$. Ferromagnetic materials have nonlinear forms. The magnetic flux in each case was measured and used to plot the magnetic flux density curve. The magnetizing force $H_{(t)}$ (A/m) was determined using the following equation:

$$H_{(t)} = \frac{I_{(t)} \cdot N_1}{l} \tag{2}$$

where N_1 is the number of turns in the coil, $I_{(t)}$ is the input current flowing through the coil, and l is the length of the magnetic material. The output signal (EMF) is obtained as a voltage and can be converted to $B_{(t)}$ (magnetic flux density, T) through electromagnetic induction and Lenz's law, as shown in the following equation:

$$B_{(t)} = -\frac{1}{AN_2} \int_{t_0}^{t_1} \frac{d\epsilon_{(t),2}}{dt} \cdot dt \tag{3}$$

where $\epsilon_{(t),2}$ is the induced EMF in the second coil from time t_0 to t_1, N_2 is the number of turns in the second coil, and A is the cross-sectional area of the steel rod. In this study, the magnetic flux through the air gap was neglected because the permeability of vacuum was much smaller than that of the steel rod.

B. Damage Detection

Magnetostriction is the property of certain materials, wherein the shape of the material changes in response to a magnetic field. Specifically, when a magnetic field is applied to a magnetostrictive material, the length or shape of the material changes owing to the reorientation of its magnetic domains. Fig. 2 shows the variation in the magnetic history owing to the physical changes in the ferromagnetic material. An electrical signal can be obtained by measuring the changes in the magnetic history using an EM sensor; thus, the physical changes in ferromagnetic materials can be estimated [32], [33].

A magnetic field is generated when the input current flows through the first coil. The magnetic flux passing through the sensor can be divided into two components: one component flows through the steel rod and the other flows through the air gap [34]

$$\epsilon_{(t)} = -N_2 \frac{d\left(\Phi_{\text{core}} + \Phi_{\text{air}}\right)}{dt} \tag{4}$$

where Φ_{core} is the magnetic flux passing through the core, and Φ_{air} denotes the magnetic flux through the air.

As shown in Fig. 3, if damage occurs at A_2 on a steel rod with a cross-sectional area of A_1, the effective cross-sectional

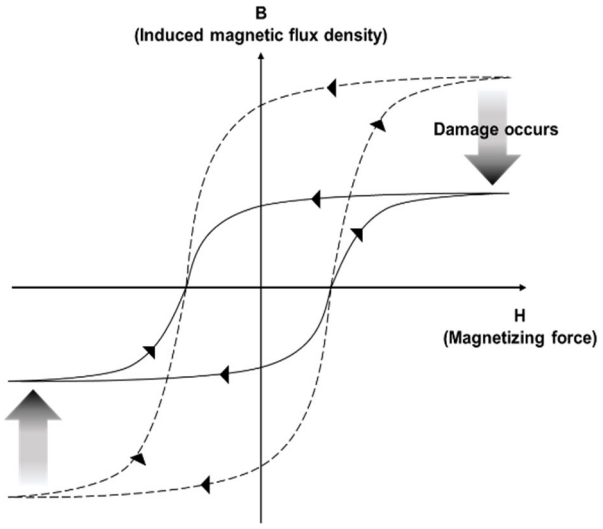

Fig. 2. Change in magnetic properties of ferromagnetic material due to the occurrence of damage.

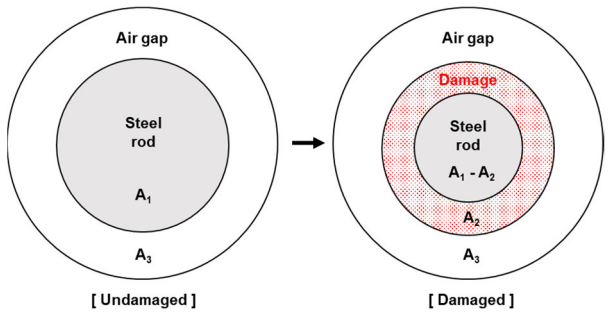

Fig. 3. Schematic of change in cross-sectional area due to damage.

area of the steel rod decreases by $A_1 - A_2$. Despite the disorderly occurrence of damage in actual field, the circular ring representation enables establishing the relationship between area reduction and damage. Hence, this study was conducted with the assumption that damage occurs uniformly in all directions of the steel tendon

$$\sum \Phi_{(t),\text{undamage}} = A_1 \cdot B_c + \mu_0 \cdot A_3 \cdot H_{(t)} \tag{5}$$

$$\epsilon_{(t),\text{undamage}} = -N \frac{\sum \Phi_{(t),\text{undamage}}}{dt} \tag{6}$$

$$\epsilon_{(t),\text{damage}} = -N \frac{d\left(A_1 \cdot B_c + \mu_0 \cdot A_3 \cdot H_{(t)}\right)}{dt} \tag{7}$$

$$\sum \Phi_{(t),\text{damage}} = (A_1 - A_2) \cdot B_c + A_2 \cdot B_d + \mu_0 \cdot A_3 \cdot H_{(t)} \tag{8}$$

where $A_1 - A_2 = A_d$

$$\epsilon_{(t),\text{damage}} = -N \frac{\sum \Phi_{(t),\text{damage}}}{dt} \tag{9}$$

$$\epsilon_{(t),\text{damage}} = -N \frac{d\left(A_d \cdot B_c + A_2 \cdot B_d + \mu_0 \cdot A_3 \cdot H_{(t)}\right)}{dt} \tag{10}$$

where $\sum \Phi_{(t),\text{undamage}}$ and $\sum \Phi_{(t),\text{damage}}$ denote the total sum of magnetic flux passing through the sensor without and with damage, respectively. B_c and B_d denote the magnetic flux passing through the tendon and damage area, respectively.

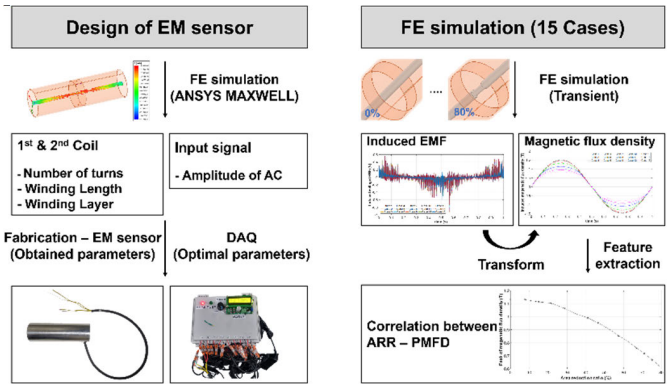

Fig. 4. Process of EM sensor design and FE simulation.

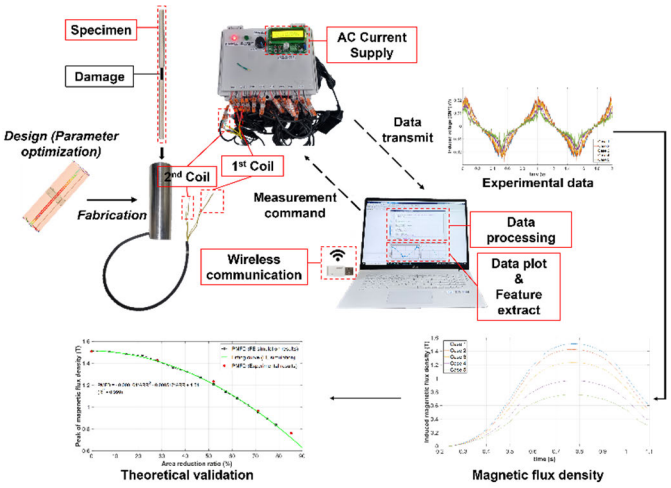

Fig. 5. Procedure of experiment and theoretical validation.

μ_0 is the vacuum permeability with a magnitude of 1.2566×10^{-6} A/m^2. Thus, the amount of magnetic flux linkage passing through the EM sensor changes, as shown in (8). This induces a change in the EMF, as shown in (9) and (10).

III. Methodology

This study proposes an NDE technique for an embedded tendon in a ground anchor. A design process considering the electromagnetic characteristics of the materials and target object is necessary to fabricate an EM sensor. Therefore, the parameters of the EM sensor used for the indoor experiment were optimized through an FE simulation. Subsequently, the EM sensor was modeled by applying the optimized parameters. Fig. 4 shows the flow of the design process and FE simulation. FE simulations were performed for 15 different cases to analyze the changes in magnetic hysteresis with respect to the area reduction ratio (ARR)

$$\text{ARR} = \frac{A_1 - A_2}{A_1} \times 100\,(\%) \tag{11}$$

where ARR is the area reduction ratio of steel rod. A_1 and A_2 denote the cross-sectional area of steel rod before damage and cross-sectional area, where the damage occurred, respectively.

Finally, the relationship between the ARR and peak magnetic flux density (PMFD) was derived from the FE simulation results. The EM sensor was fabricated by applying the optimized parameters to verify the damage detection potential of the EM sensor. Subsequently, the fabricated EM sensor was used to measure the damage in five cases, and the induced EMF data were extracted from the measurements. The time–magnetic flux density curve was plotted using the EMF data, and the PMFDs were extracted. The measurement reliability was validated by comparing the results obtained from the FE simulations with the experimental data. Fig. 5 shows the experimental and theoretical validation procedures.

IV. Design of EM Sensor

A. Ansys Maxwell

ANSYS Maxwell, used for the FE simulation in this study, is an electromagnetic FE simulation software program based on Maxwell's equations. Also, it is designed to incorporate the eddy current effects during the 3-D modeling process. Specifically, components within the simulations are configured to consider the eddy current effect. Additionally, the magnetic hysteresis of the SS400 steel tendon has been assigned to the material properties for conducting FE simulations. Using the Kelvin–Stokes theorem, based on which a measurement simulation of the actual EM sensor can be performed [35], [36], the Maxwell–Faraday equation can be expressed as follows:

$$\nabla \times E = -\frac{dB}{dt} \tag{12}$$

$$\int_{\partial\Sigma} E \cdot dl = -\int_{\Sigma} \frac{\partial B}{\partial t} \cdot dA \tag{13}$$

where $\nabla\times$ is the curl operator, E is the electric field, and B is the magnetic field. In addition, according to Stoke's theorem, Σ denotes the surface of a differentiable manifold, and $\partial\Sigma$ denotes the closed boundary curve. dA is an infinitesimal vector element of surface Σ. dl is an infinitesimal vector element of the contour $\partial\Sigma$.

B. Three-Dimensional Model Description

Before the analysis, three-dimensional (3-D) modeling of the steel rod and EM sensor comprising the sensor head and first and second coils was conducted, as shown in Fig. 6. Compared with a two-dimensional (2-D) analysis, a 3-D analysis has the disadvantage of a long computational time because it analyzes more elements; nonetheless, it is more precise than a 2-D analysis.

The winding length and diameter were assigned fixed values, taking into consideration their combination with the actual ground anchor sheath. The parameters were set as the winding length and number of turns, which directly affect the magnitude of the magnetizing force generated by the first coil and EMF induced in the second coil. The first coil that inputs the current was 200 mm long, with T_{1_i} turns and an 83.0 mm inner diameter. The second coil that receives the induced EMF from the magnetized steel rod was 30 mm long, with T_{2_i} turns and an 82.4 mm inner diameter. Each coil was then wound onto the N_{1_i} and N_{2_i} layers. Table I lists the details of the properties and parameters of the coil in EM sensor.

TABLE I
PROPERTIES AND PARAMETERS OF EM SENSOR OF THE COIL

Parameter	1st coil	2nd coil
Materials	Copper	
Relative Permeability	0.999991	
Bulk Conductivity	103/5.80 siemens/m	
Mass Density	8933 kg/m3	
Diameter	83.0 mm	82.4 mm
Thickness	1.2 mm	0.2mm
Resistance	2.36 ohm	10.3 ohm
Winding Length	200 mm	30 mm
Winding Layer	T_{1_i}	T_{2_i}
Number of Turns	N_{1_i}	N_{2_i}
Self-inductance	L_1	L_2

TABLE II
PROPERTIES OF SS400 CYLINDRICAL STEEL ROD

Parameter	Properties	
Mechanical properties	Yield Strength(f_y)	245 MPa
	Tensile Strength(p_u)	450 MPa
	Mass Density	7850 kg/m^3
	Diameter	13 mm
	Length	300 mm
Electrical properties	Electrical Resistivity	0.00002 ohm·cm^2/cm
	Bulk Conductivity	4.17x106 siemens/m

Coil inductances L_1 and L_2 are critical to the performance of the EM sensor measurement. The values of the other parameters are used to determine coil inductance as follows:

$$L = \frac{\mu_r \cdot \mu_0 \cdot N \cdot A}{l} \tag{14}$$

where L is the self-inductance of coil. μ_r and μ_0 denote the relative permeability of the steel rod and magnetic permeability in a classical vacuum, respectively. N denotes the number of coil turns, A is the cross section area, and l is the length of coil.

Mutual inductance is automatically reflected in the simulation [37], [38].

A high-durability acrylic material was used for the sensor head without affecting the electromagnetic measurement of the EM sensor, considering the influence of field installation. The specifications of the sensor head were designed by considering the actual ground anchor and its sheath. An SS400 cylindrical steel rod, typically used for ground anchor tendons in South Korea, was used for the specimen. Table II lists the properties of SS400 cylindrical steel rod, including the physical and electrical properties.

In addition, considering the size of the actual ground anchor and calculating the sensor parameter values are necessary for applying an EM sensor in the field. Thus, this study adjusted the sensor size for indoor experiments.

C. Alternating Voltage Magnetization

This study used the transient analysis of an EM sensor to extract the magnetic flux for each steel rod. As shown in

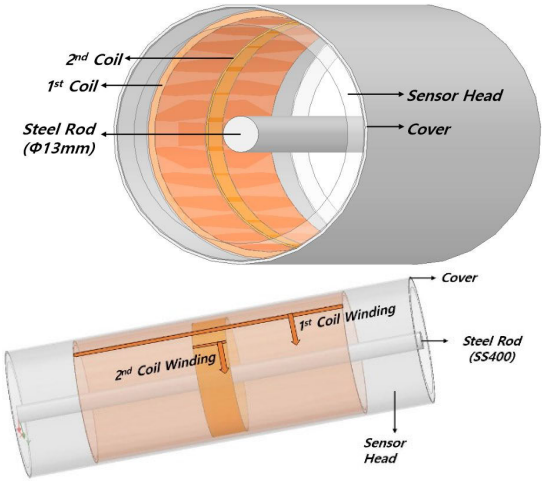

Fig. 6. Three-dimensional modeling of EM sensor and steel rod.

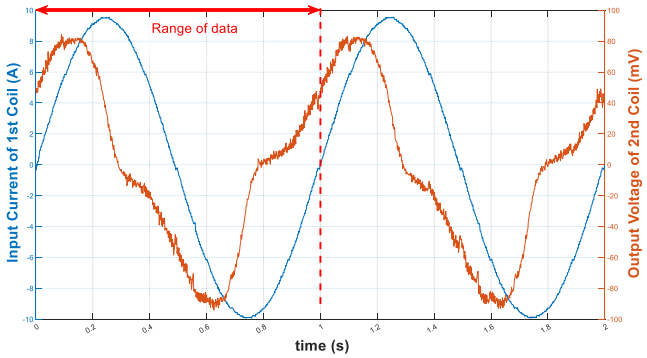

Fig. 7. Input current in the first coil and induced voltage in the second coil.

Fig. 7, a sine wave ac signal was used to plot the magnetic flux density curve of the steel rod. A magnetic field was generated when an input current was applied to the first coil, saturating the steel rod. The magnetic flux generated as a sine wave from the steel rod through the second coil induced the EMF. The magnetic flux density was obtained by integrating the EMF with respect to time.

The data acquisition (DAQ) system used in this study can receive 1500 samples in 2 s for each of the first and second coils and can measure for two cycles. The measured signal's shape shows that the frequency of the sinusoidal is 1.0 Hz. The data employed for the analysis of the experimental data correspond only to a one cycle of a total of two cycles; specifically, 770 data points were extracted to obtain one cycle of the magnetic flux density curve. The time range corresponding to extracted data is from 0.233 to 1.026 s. This is because a one cycle of EMF is necessary to obtain one cycle of induced magnetic flux density. In the case of FE simulation, the input signal corresponding to the actual experiment was used for the period specified (0.233–1.026 s). To analyze the change in the magnetic hysteresis according to the localized damage of the steel rod, determining the parameters of the input signal that can saturate the SS400 steel rod was necessary to observe a clear change in the magnetic hysteresis. When tendon damage occurs, the amount of magnetic flux generated

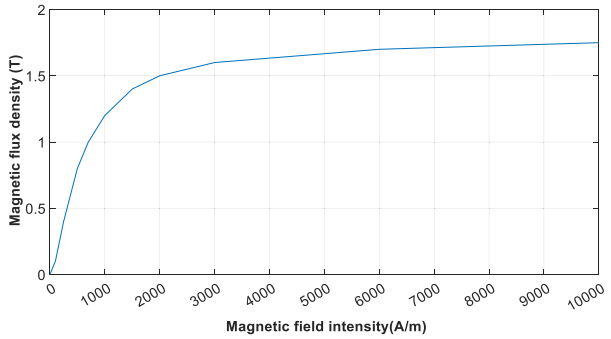

Fig. 8. B–H curve of SS400 steel rod.

is lower than that in the undamaged state, causing the tendon to saturate more rapidly. Therefore, identifying the saturation point in an undamaged state is essential. Fig. 8 shows the B–H curve of the SS400 steel. The figure shows that the steel rod was saturated when the magnetic flux density was between 1.5 and 1.6 T.

D. Optimization of EM Sensor Parameters

According to the definition of the magnetizing force, the saturation of a ferromagnetic material depends on parameters, such as the number of turns in the coil and layers of the coils. Other parameters, including the winding length, diameter, shape of the input signal, and current amplitude, were default. The design parameters of the EM sensor, such as the number of turns and winding layers of the coils, were determined with the coil winding. When installing ground anchors on the actual site, there is a concern that designing the diameter of the first coil larger than the sheath's diameter could potentially lead to the cutting of the coil. If the size of the sensor is larger than that of the sheath, the sensor could get damaged during installation. Therefore, to ensure installation convenience and prevent the cutting of the first coil, it is advantageous to minimize the size of the EM sensor. Additionally, to facilitate the coupling with the sheath, the winding layer has been set to a maximum of 2. Table III lists the parameter setting of the first and second coil windings for each case. In addition, the coil diameter was calculated by considering the coupling with the ground anchor sheath [30].

As shown in Fig. 9, the FE simulation results indicate that the magnetic flux density increased with the number of windings in the first coil. In NDE techniques using electromagnetic sensors, the saturation point of the target object is a crucial indicator of a presence or absence of a damage. In Cases 2 and 4, the maximum value of the magnetic flux density was approximately 0.75 T, which indicates that it is not sufficient to saturate the SS400 steel rod. In Cases 1 and 3, the magnetic flux density reached 1.51 T at 0.25 s after signal input, which is sufficient to saturate the SS400 steel rod. Increasing the number of coil winding turns improved the sensitivity and resolution of the sensor. Thus, Case 3 with more first coil windings was adopted, as shown in Table IV.

The intensity of the magnetic field can be expressed, as shown in Fig. 10. The distribution of the magnetic field of the sensor can be calculated by applying the design parameters

TABLE III
CASE OF WINDING PARAMETERS

Coil	Parameters	Case 1	Case 2	Case 3	Case 4
1st coil	Length	200 mm			
	Layer	1	1	2	2
	Turns	165	165	330	330
	Diameter (Outer)	83 mm			
	Thickness	1.2 mm		2.4 mm	
	Self-inductance	0.0926 H		0.3700 H	
2nd coil	Length	30 mm			
	Layer	1	2	1	2
	Turns	76	146	76	146
	Diameter (Outer)	82.4 mm			
	Thickness	0.2 mm	0.4 mm	0.2 mm	0.4 mm
	Self-inductance	0.1270 H	0.4760 H	0.1270 H	0.4760 H

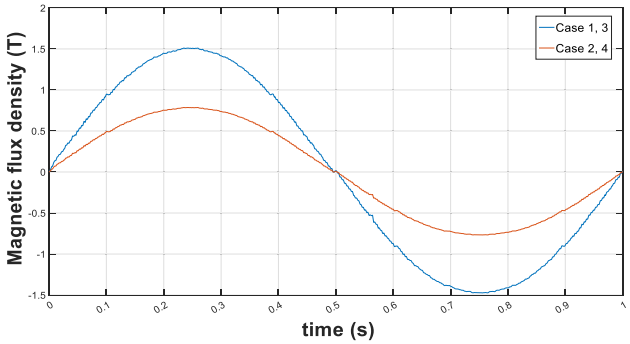

Fig. 9. Magnetic flux density according to the coil winding parameters (FE simulation results).

TABLE IV
OPTIMIZED WINDING PARAMETERS (CASE 3)

Parameter	1st coil	2nd coil
Thickness	1.2 mm	0.2mm
Resistance	2.36 ohm	10.3 ohm
Winding Length	200 mm	30mm
Winding Layer	$T_{1\_i} = 2$	$T_{2\_i} = 1$
Number of Turns	$N_{1\_i} = 330$	$N_{2\_i} = 76$
Amplitude of input current	10 A	

of Case 3 and its intensity. The maximum magnetic flux density through the steel rod was approximately 1.58 T, sufficient to saturate the 300-mm-long, 13-mm-diameter SS400 steel rod.

V. EXPERIMENTAL SETUP

In this study, indoor experiments were performed at the range of 23.1 °C–23.9 °C to verify the capability and sensitivity of the fabricated EM sensor for detecting tendon damage.

The parameters related to the coil winding and input current were applied using the parameters obtained through

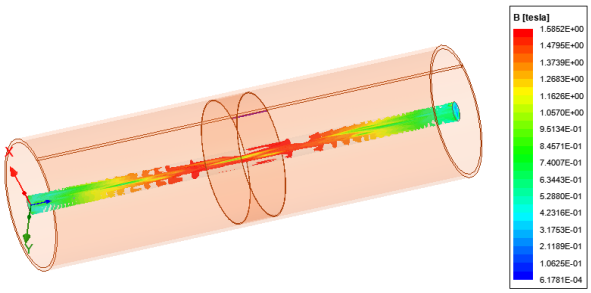

Fig. 10. Magnetic flux density in the steel rod of applying optimized parameters (Case 3).

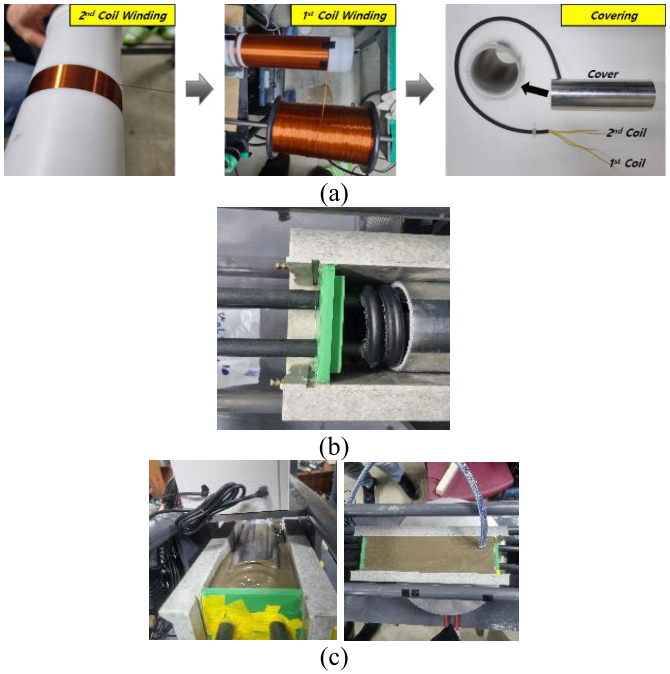

Fig. 11. (a) Manufacturing of EM sensor. (b) Combining with sheath. (c) Grouting.

the simulation. Table IV lists the parameters obtained from optimization process (Case 3). The sensor head was designed and fabricated based on the actual shape of a ground anchor, as shown in Fig. 11(a). It was designed as an integral type to connect to the ground anchor sheath for installation at an actual site, as shown in Fig. 11(b). Adding screw threads to the sensor head based on the sheath specifications ensured that the sensor remained stationary during installation, resulting in highly reliable data under actual field conditions.

In addition, the EMF before and after grouting was analyzed to assess the influence of concrete grouting on the measurement signals because concrete grouting is typically performed during the on-site construction of ground anchors, as shown in Fig. 11(c).

SS400 steel rods with 13 mm diameters, commonly used as ground anchor tendons, were used for the specimen. The experimental variables were set considering the damage level that could occur owing to the corrosion and collapse of the steel wires in the steel strands. The damage in the shape of the steel rod was not uniform. However, the specimens

Fig. 12. Specimens for the indoor experiment (SS400 cylindrical steel rod).

TABLE V
SPECIFICATIONS OF THE SPECIMEN

Case No.	Diameter (D) of specimen In damage section (mm)	Cross-sectional area(mm2)	Area reduction ratio (%)
1	13	132.73	0
2	11	95.03	28.40
3	9	63.62	52.07
4	7	38.48	71.01
5	5	19.63	85.21

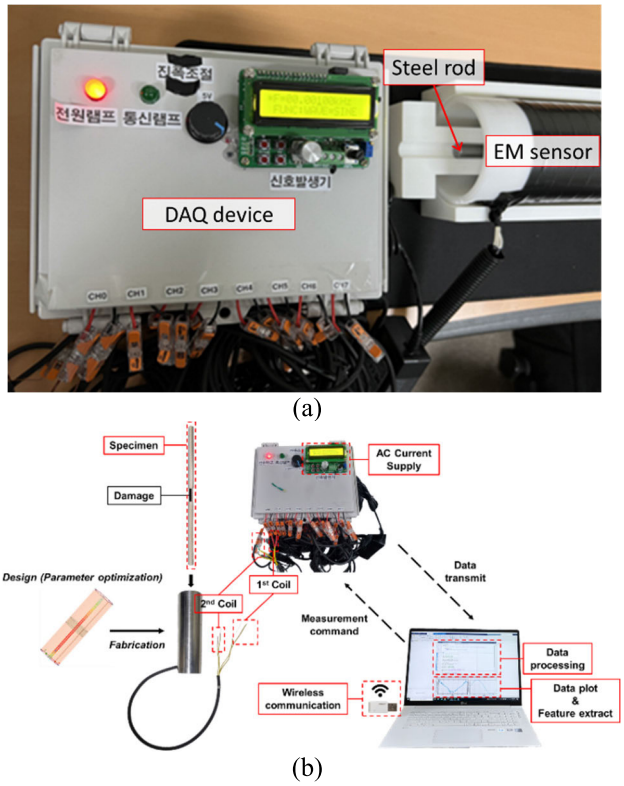

Fig. 13. (a) Experimental setup and (b) measurement flow of damage detection.

simulating local damage were fabricated under the assumption of uniform damage in all directions to quantitatively analyze the correlation between damage and induced magnetic flux density. The specimens were produced by simulating sectional losses of 0%, 28.40%, 52.07%, 71.01%, and 85.21% with a 30 mm length for each tendon, as shown in Fig. 12. Table V lists the specifications of specimens for indoor experiment.

Fig. 13 shows the measurement process. The process was controlled using a computer with a DAQ device, comprising

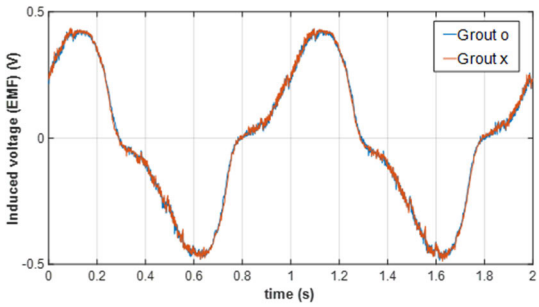

Fig. 14. Results of grouting experiment.

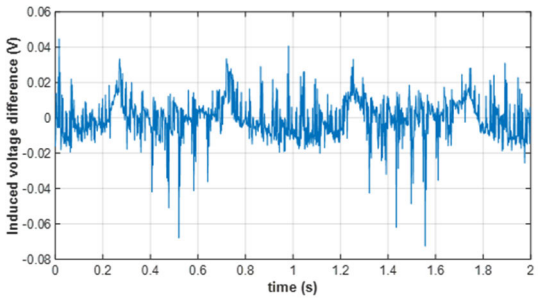

Fig. 15. Differences of induced EMF before and after grouting.

D/A and A/D converters. The input current was a sinusoidal ac with a 1.0-Hz frequency, and 1501 data samples were processed within 2 s. Subsequently, 770 data points were extracted to obtain one cycle of the magnetic flux density curve, corresponding to data from 0.233 to 1.026 s. The input current flowed through the first coil when a measurement command was input to the computer, and the magnetic flux was generated in the specimen. Consequently, the induced EMF in the second coil was measured by the DAQ device through wireless communication. The data obtained from ten times measurements were averaged for the consideration of measurement errors. The peak of the magnetic flux density for each case was extracted from the obtained signals to analyze the change in hysteresis that occurred as the damage to the specimen increased.

VI. Experimental Validation

A. Experimental Results

Temperature compensation is essential to an EM sensor that transmits and receives signals via a coil to account for significant signal variation caused by changes in the external temperature. The external temperature was maintained within the range of 23.1 °C–23.9 °C during the measurements to prevent any influence due to temperature.

To analyze the effect of grouting on the measurement signal, grouting experiment was conducted after five days of concrete grout curing. Figs. 14 and 15 show the results. The average difference was 0.00046 V, and the maximum signal difference before and after grouting was less than 1%. This indicates the negligible effect of concrete grouting on the measurements.

As shown in Fig. 16(a), the time–EMF curve for each damage case was obtained under different damage levels. The shape of the induced EMF curve changed as the level of damage to the specimen changed. The magnetic flux density was derived from the induced EMF for each case, as shown in Fig. 16(b).

Table VI shows the experimental results. The PMFD decreased as the level of damage to the specimen increased. This was because of the difference in the alignment amount of the atomic spin within the same range of magnetizing force, causing a difference in the total magnetic flux density for each specimen. The decrease in the effective cross-sectional area owing to damage reduced the specimen volume. Consequently, the amount of magnetic flux passing through the specimen, with a significantly higher permeability than the damaged section, decreased.

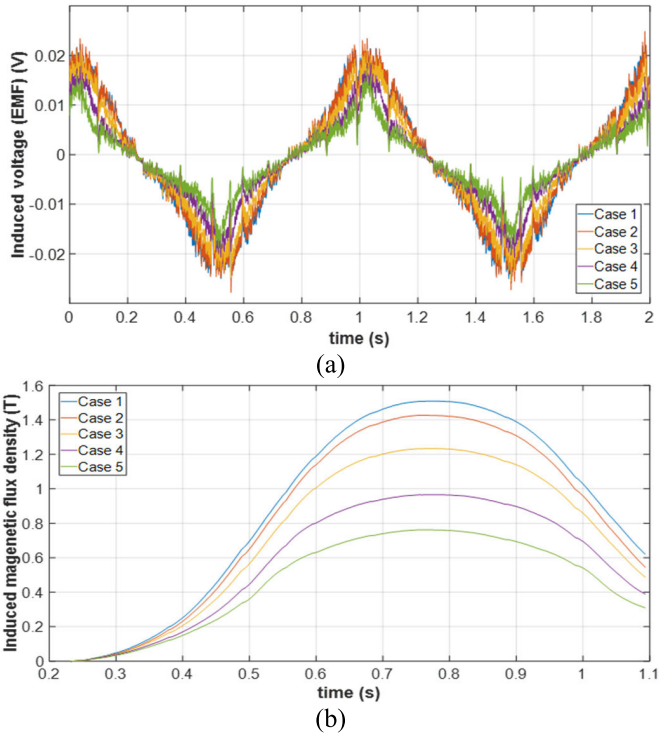

Fig. 16. (a) Induced EMF for the five cases. (b) Induced magnetic flux density for the five cases.

TABLE VI
Experimental Results: PMFD According to ARR

Case No.	ARR (Area reduction ratio) (%)	PMFD (Peak of magnetic flux density) (T)
1	0	1.509
2	28.40	1.427
3	52.07	1.233
4	71.01	0.966
5	85.21	0.762

B. Theoretical Validation Based on FE Simulation

This section performs a transient analysis through FE simulation to verify the reliability and performance of the fabricated EM sensor to calculate the induced magnetic flux density theoretically through the specimen. The maximum number of additional elements for the mesh was set to 1000 for

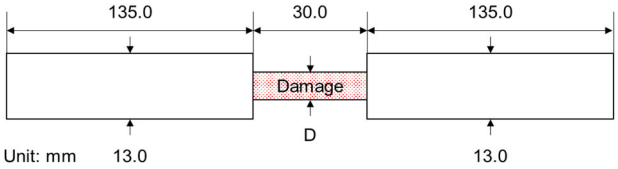

Fig. 17. Schematic illustration of damaged specimen.

TABLE VII
DAMAGE CASES FOR FE SIMULATION

Case No.	Diameter (D) of specimen in damage section (mm)	Cross-sectional area (mm^2)	Area reduction ratio (%)
1	13.0	132.73	0
2	12.5	122.72	7.54
3	12.0	113.10	15.09
4	11.5	103.87	21.75
5	11.0	95.03	28.40
6	10.5	86.59	34.76
7	10.0	78.54	40.83
8	9.5	70.88	46.60
9	9.0	63.62	52.07
10	8.5	56.75	57.25
11	8.0	50.27	62.13
12	7.5	44.18	66.72
13	7.0	38.48	71.01
14	6.5	33.18	75.00
15	6.0	28.27	78.70

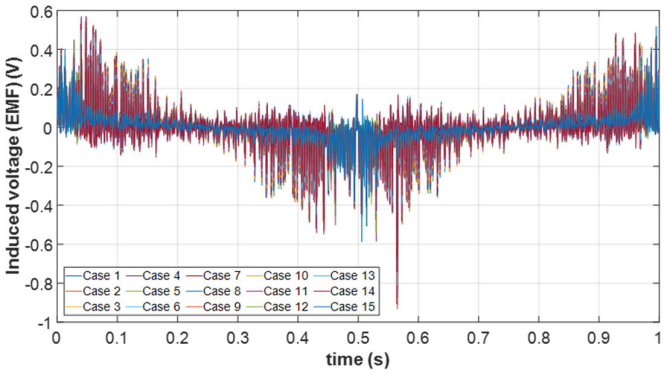

Fig. 18. Induced EMF for each case by FE simulation.

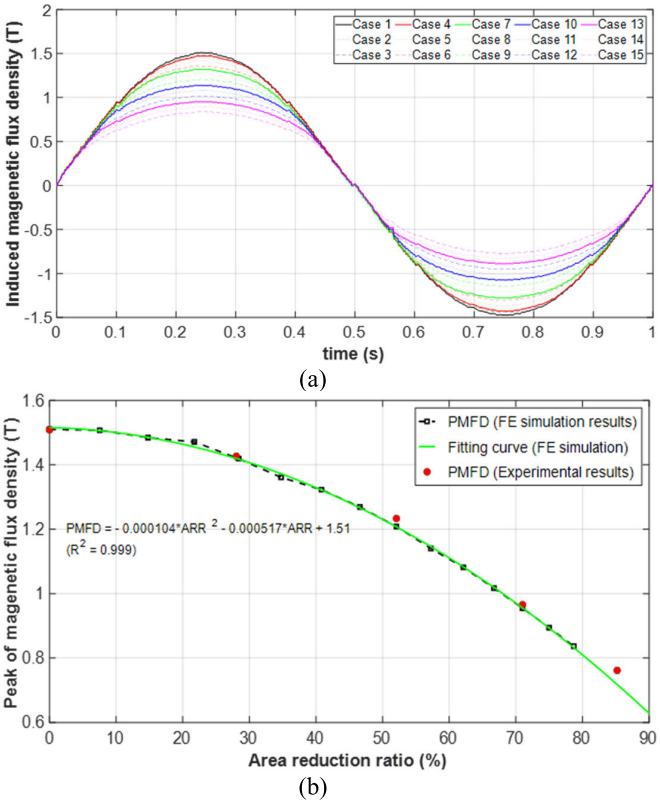

Fig. 19. (a) Magnetic flux density for each case and (b) comparison of FE simulation results with experimental results: peak of magnetic flux density (PMFD) versus ARR curve.

TABLE VIII
COMPARISON OF EXPERIMENT AND FE SIMULATION RESULTS

Case No.	ARR	PMFD (FE simulation) (T)	PMFD (Experiment) (T)	Error (%)
1	0	1.510	1.509	0.0871
2	28.40	1.411	1.427	1.0728
3	52.07	1.201	1.233	2.6931
4	71.01	0.949	0.966	1.7524
5	85.21	0.711	0.762	7.1685

all components. Thus, the number of elements in the 3-D modeling meshes was 1000 for all components, sufficient for an accurate analysis. In addition, ac current with 10 A is used as an input in the experiment applied in the simulation as well. The analysis was conducted for 15 damage cases, decreasing the diameter of the specimen gradually by 0.5 mm. Fig. 17 and Table VII show the specifications for each damage case.

Fig. 18 shows the time–EMF curve for each damage case. However, significant noise limited the data analysis, making it challenging to extract a specific index representing each damage case. To overcome this limitation, the induced EMF data were transformed into the magnetic flux density based on the electromagnetic induction principle, as shown in (3). Fig. 19(a) shows the time–magnetic flux density curve for each damage case obtained from the time–EMF curve.

As shown in Table VIII, the FE simulation results indicated that the magnetic flux density decreased as the damage level increased. The peaks were extracted from the magnetic flux density curves for each case, as shown in Fig. 19(b). The PMFD and ARR exhibited a quadratic relationship could be fitted as (15)

$$\text{PMFD} = 0.000104 \times \text{ARR}^2 - 0.000517 \times \text{ARR} + 1.51. \tag{15}$$

The correlation coefficient (R) of in the quadratic regression equation was 0.999.

Fig. 19(b) compares the experimental results with the quadratic regression curves obtained from the FEM simulation results. The average error was 2.55%, with the maximum at approximately 7.17%. The difference between the experiment and FE simulation results can be attributed to various factors. External environments beyond the designated area were not considered in the simulations. Thus, in an actual experiment, the presence of surrounding objects affects the behavior of the magnetic field, making it challenging to obtain results

consistent with the simulation results. The thermal resistances of the first and second coils used in the FE simulations were the theoretical resistances. However, in an actual EM sensor, the coil temperature changes with every measurement and directly affects the EMF induced by the DAQ [38], [39], [40].

VII. Conclusion

Detecting tendon damage is critical for ensuring the safety and stability of embedded structures, such as ground anchors. The stability of the structure supported by the ground anchor may be compromised if corrosion or local damage occurs in the tendon or the wire of the steel strand breaks during the service life of the ground anchor. In the worst case scenarios, this can lead to sudden structural collapse and potential loss of life. However, studies on damage detection techniques for ground anchor tendons are limited.

This study proposed a damage detection method based on the measurement of induced EMF using an EM sensor. The magnetic saturation point of the material and optimal EM sensor parameters must be determined to accurately analyze the magnetic hysteresis of a magnetic material using an EM sensor. Accordingly, the sensor parameters were initially determined through an FE simulation, considering the size and form of an actual ground anchor. Indoor experiments were performed at room temperature to verify the capability and sensitivity of the fabricated EM sensor for detecting tendon damage by applying parameters obtained from the FE simulation. Finally, the FE simulation and experiment results were compared.

1) A 3-D electromagnetic FE simulation (ANSYS MAXWELL) was conducted to obtain the optimal parameters for the EM sensor. Using a fixed ac with a peak of 10.0 A, a time-domain analysis was performed by setting the parameters related to the first and second coils as variables. The induced EMF was obtained for each case through transient analysis. Subsequently, the results were used to determine the parameters that could saturate a 300-mm-long, 13-mm-diameter SS400 cylindrical steel rod.
2) An eddy current solver was used by applying the optimized parameters (Case 3) to confirm the magnetic flux distribution of the specimen. The peak value of the magnetic flux density through the specimen reached 1.58 T. This value was selected as the design parameter for the EM sensor.
3) The magnetic flux density curve for each damage case was obtained at different damage levels (five cases). The PMFD was derived from the induced EMF in each case. The results indicated that the level of damage to the specimen increased, and the PMFD decreased. This was because of the difference in the alignment amount of the atomic spin within the same range of magnetizing force.
4) A transient analysis through FE simulation was performed to verify the reliability and performance of the fabricated EM sensor. The PMFD and ARR exhibited a quadratic relationship. A comparison of the FE simulation and experimental results indicated average and maximum errors of 2.55% and approximately 7.17%, respectively. A significant error was observed in Case 5. This was because the damage level was beyond the range set in the FE simulation.

In addition, owing to the excellent forming properties of EM sensors, the proposed method can be applied to ground anchors and any structure comprising metallic materials. The proposed design method and NDE technique for EM sensors serve as a foundational reference for future research on damage detection in metallic materials. In summary, this study analyzed the changes in magnetic flux density based on area reduction to detect local damage in tendons. The proposed method involves analyzing the correlation between ARR and PMFD, assuming that damage to the steel rod occurs exactly in line with the center of EM sensor. If the damage were to occur at a different location, it would still be possible to detect the occurrence of damage itself. However, obtaining an accurate ARR would be challenging. Therefore, our research team is currently conducting a study that integrates the MFL technique with the EM sensor to identify the location of damage occurrence and quantitatively assess the ARR. Furthermore, through the integration with the MFL technique, we anticipate the capability to detect not only the ARR but also the length of damage along the steel rod.

Acknowledgment

Dongyoung Ko and Changjun Lee are with the Department of Global Smart City, Sungkyunkwan University, Suwon 16409, Republic of Korea (e-mail: ehddud3555@skku.edu; russel4447@skku.edu).

Jooyoung Park is with the Department of Civil and Environmental System Engineering, Sungkyunkwan University, Suwon 16409, Republic of Korea (e-mail: mitjy26@gmail.com).

Junkyeong Kim is with Safety Inspection for Infrastructure Laboratory, Advanced Institute of Convergence Technology, Suwon 16229, Republic of Korea (e-mail: junkyeong@snu.ac.kr).

Hyungchul Yoon is with the Department of Civil Engineering, Chungbuk National University, Cheongju 28644, Republic of Korea (e-mail: hyoon@cbnu.ac.kr).

Seunghee Park is with the School of Civil, Architectural Engineering and Landscape Architecture, Sungkyunkwan University, Suwon 16409, Republic of Korea (e-mail: shparkpc@skku.edu).

References

[1] N.-K. Kim, J.-S. Park, and S.-K. Kim, "Numerical simulation of ground anchors," in *Computer and Geotechnics*, vol. 34, no. 6. Amsterdam, The Netherlands: Elsevier, Nov. 2007, pp. 498–507, doi: 10.1016/j.compgeo.2006.09.002.

[2] P. P. Xanthakos, "Corrosion and corrosion protection," in *Ground Anchors and Anchored Structures*. Washington, DC, USA: Wiley, 1991, pp. 240–293.

[3] P. J. Sabatini, D. G. Pass, and R. C. Bachus, "Corrosion considerations in design," in *Ground Anchors and Anchored Systems*. Washington, DC, USA: Federal Highway Administration, 1999, pp. 124–136.

[4] A.-J. Li, H.-C. Wen, V. H. Batistuta, and S.-H. Cheng, "Influence of ground anchors corrosion and uncertainty strength parameters: A case study slope failure in northern Taiwan," in *Soils and Foundations*, vol. 63, no. 3. Amsterdam, The Netherlands: Elsevier, Jun. 2023, doi: 10.1016/j.sandf.2023.101316.

[5] W. H. Hartt, "Effect of modeling variables upon projection of corrosion-induced bridge post-tension tendon failures," *Corrosion*, vol. 74, no. 7, pp. 768–775, Jul. 2018, doi: 10.5006/2710.

[6] V. Giurgiutiu, "Embedded non-destructive evaluation for structural health monitoring, damage detection, and failure prevention," *Shock Vib. Dig.*, vol. 37, no. 2, pp. 83–105, Mar. 2005, doi: 10.1177/0583102405052561.

[7] J. Kim and S. Park, "Field applicability of a machine learning–based tensile force estimation for pre-stressed concrete bridges using an embedded elasto-magnetic sensor," *Struct. Health Monitor.*, vol. 19, no. 1, pp. 281–292, Jan. 2020, doi: 10.1177/1475921719842340.

[8] T. A. Baudendistel and M. L. Turner, "A novel inverse-magnetostrictive force sensor," *IEEE Sensors J.*, vol. 7, no. 2, pp. 245–250, Feb. 2007, doi: 10.1109/JSEN.2006.886876.

[9] B. Silva, R. M. Fisher, A. Kumar, and G. P. Hancke, "Experimental link quality characterization of wireless sensor networks for underground monitoring," *IEEE Trans. Ind. Informat.*, vol. 11, no. 5, pp. 1099–1110, Oct. 2015, doi: 10.1109/TII.2015.2471263.

[10] J.-Z. Su et al., "Long-term structural performance monitoring system for the Shanghai tower," *J. Civil Struct. Health Monitor.*, vol. 3, no. 1, pp. 49–61, Jan. 2013, doi: 10.1007/s13349-012-0034-z.

[11] Z. Sun, P. Wang, M. C. Vuran, M. A. Al-Rodhaan, A. M. Al-Dhelaan, and I. F. Akyildiz, "MISE-PIPE: Magnetic induction-based wireless sensor networks for underground pipeline monitoring," *Ad Hoc Netw.*, vol. 9, no. 3, pp. 218–227, May 2011, doi: 10.1016/j.adhoc.2010.10.006.

[12] S. Kisseleff, I. F. Akyildiz, and W. H. Gerstacker, "Survey on advances in magnetic induction-based wireless underground sensor networks," *IEEE Internet Things J.*, vol. 5, no. 6, pp. 4843–4856, Dec. 2018, doi: 10.1109/JIOT.2018.2870289.

[13] M. Li and Y. Liu, "Underground structure monitoring with wireless sensor networks," in *Proc. IPSN*, vol. 7, Apr. 2007, pp. 69–78, doi: 10.1145/1236360.1236370.

[14] I. F. Akyildiz and E. P. Stuntebeck, "Wireless underground sensor networks: Research challenges," *Ad Hoc Netw.*, vol. 4, no. 6, pp. 669–686, Nov. 2006, doi: 10.1016/j.adhoc.2006.04.003.

[15] B. Zima, and M. Rucka, "Wave propagation in damage assessment of ground anchors," presented at the 11th Int. Conf. Damage Assessment Struct., Ghent, Belgium, vol. 628, 2015, doi: 10.1088/1742-6596/628/1/012026.

[16] X. C. Liu, J. W. Xiao, B. Wu, and C. F. He, "A novel sensor to measure the biased pulse magnetic response in steel stay cable for the detection of surface and internal flaws," *Sens. Actuators A, Phys.*, vol. 269, pp. 218–226, Jan. 2018, doi: 10.1016/j.sna.2017.11.005.

[17] X. Yan, D. Zhang, and F. Zhao, "Improve the signal to noise ratio and installation convenience of the inductive coil for wire rope nondestructive testing," *NDT & E Int.*, vol. 92, pp. 221–227, Dec. 2017, doi: 10.1016/j.ndteint.2017.09.005.

[18] G. Fedorko, V. Molnár, Ž. Ferková, P. Peterka, J. Krešák, and M. Tomašková, "Possibilities of failure analysis for steel cord conveyor belts using knowledge obtained from non-destructive testing of steel ropes," *Eng. Failure Anal.*, vol. 67, pp. 33–45, Sep. 2016, doi: 10.1016/j.engfailanal.2016.05.026.

[19] A. Vallan and F. Molinari, "A vision-based technique for lay length measurement of metallic wire ropes," *IEEE Trans. Instrum. Meas.*, vol. 58, no. 5, pp. 1756–1762, May 2009, doi: 10.1109/TIM.2009.2012953.

[20] O. Yaman and M. Karakose, "Auto correlation based elevator rope monitoring and fault detection approach with image processing," in *Proc. Int. Artif. Intell. Data Process. Symp. (IDAP)*, Malatya, Turkey, Sep. 2017, pp. 16–17, doi: 10.1109/IDAP.2017.8090176.

[21] E.-S. Wacker and J. Denzler, "Enhanced anomaly detection in wire ropes by combining structure and appearance," *Pattern Recognit. Lett.*, vol. 34, no. 8, pp. 942–953, Jun. 2013, doi: 10.1016/j.patrec.2013.01.025.

[22] L. M. Sanchez-Brea, P. Siegmann, M. A. Rebollo, and E. Bernabeu, "Optical technique for the automatic detection and measurement of surface defects on thin metallic wires," *Appl. Opt.*, vol. 39, no. 4, pp. 539–545, 2000, doi: 10.1364/AO.39.000539.

[23] R. Raišutis, R. Kažys, L. Mažeika, E. Žukauskas, V. Samaitis, and A. Jankauskas, "Ultrasonic guided wave-based testing technique for inspection of multi-wire rope structures," *NDT & E Int.*, vol. 62, pp. 40–49, Mar. 2014, doi: 10.1016/j.ndteint.2013.11.005.

[24] Z. Liu, J. Zhao, B. Wu, Y. Zhang, and C. He, "Configuration optimization of magnetostrictive transducers for longitudinal guided wave inspection in seven-wire steel strands," *NDT & E Int.*, vol. 43, no. 6, pp. 484–492, Sep. 2010, doi: 10.1016/j.ndteint.2010.05.003.

[25] F. Treyssède and L. Laguerre, "Investigation of elastic modes propagating in multi-wire helical waveguides," *J. Sound Vib.*, vol. 329, no. 10, pp. 1702–1716, May 2010, doi: 10.1016/j.jsv.2009.11.021.

[26] H. Sohn, G. Park, J. R. Wait, N. P. Limback, and C. R. Farrar, "Wavelet-based active sensing for delamination detection in composite structures," *Smart Mater. Struct.*, vol. 13, no. 1, pp. 153–160, Feb. 2004, doi: 10.1088/0964-1726/13/1/017.

[27] G. Drummond, J. F. Watson, and P. P. Acarnley, "Acoustic emission from wire ropes during proof load and fatigue testing," *NDT & E Int.*, vol. 40, no. 1, pp. 94–101, Jan. 2007, doi: 10.1016/j.ndteint.2006.07.005.

[28] N. F. Casey, H. White, and J. L. Taylor, "Frequency analysis of the signals generated by the failure of constituent wires of a wire rope," *NDT&E Int.*, vol. 18, no. 6, pp. 583–586, Dec. 1985, doi: 10.1016/0308-9126(85)90164-6.

[29] Y. Ding, R. L. Reuben, and J. A. Steel, "A new method for waveform analysis for estimating AE wave arrival times using wavelet decomposition," *NDT & E Int.*, vol. 37, no. 4, pp. 279–290, Jun. 2004, doi: 10.1016/j.ndteint.2003.10.006.

[30] D. Jiles, "Magnetism in materials: Magnetic phenomena on the microscopic scale," in *Introduction to Magnetism and Magnetic Materials*. Boca Raton, FL, USA: CRC Press, 2016, pp. 109–317, doi: 10.1557/S0883769400045309.

[31] J. A. Stratton, "The field equations," in *Electromagnetic Theory*. Hoboken, NJ, USA: Wiley, 2007, pp. 1–82, doi: 10.1002/9781119134640.ch1.

[32] C. Cappello. D. Zonta, H. A. Laasri, B. Glisic, and M. Wang, "Calibration of elasto-magnetic sensors on in-service cable-stayed bridges for stress monitoring," *MDPI Sensors*, vol. 18, no. 2, pp. 1–15, 2018, doi: 10.3390/s18020466.

[33] M. J. Sablik and D. C. Jiles, "A model for hysteresis in magnetostriction," *J. Appl. Phys.*, vol. 64, no. 10, pp. 5402–5404, Nov. 1988, doi: 10.1063/1.342383.

[34] D. Y. Ko, J. Y. Park, C. J. Lee, J. Kim, and S. Park, "Analysis of changes in magnetic hysteresis due to localized corrosion of ground anchor tendon based on FEM simulation," *J. Korean Soc. Steel Construct.*, vol. 35, no. 1, pp. 1–10, Feb. 2023, doi: 10.7781/kjoss.2023.35.1.001.

[35] V. Suresh, A. Abudhahir, and J. Daniel, "Development of magnetic flux leakage measuring system for detection of defect in small diameter steam generator tube," in *Measurement*, vol. 95. Amsterdam, The Netherlands: Elsevier, Jan. 2017, pp. 273–279, doi: 10.1016/j.measurement.2016.10.015.

[36] D. Ongayo and M. Hanif, "Comparison of circular and rectangular coil transformer parameters for wireless power transfer based on finite element analysis," presented at the IEEE 13th Brazilian Power Electron. Conf., 1st Southern Power Electron. Conf., Fortaleza, Brazil, Feb. 2016, doi: 10.1109/COBEP.2015.7420222.

[37] H. Xiang et al., "Analysis of parameter sensitivity of induction coil launcher based on orthogonal experimental method," presented at the 17th Int. Symp. Electromagn. Launch Technol., La Jolla, CA, USA, Oct. 2014, doi: 10.1109/EML.2014.6920148.

[38] H. Xiang et al., "Analysis of parameter sensitivity of induction coil launcher based on orthogonal experimental method," *IEEE Trans. Plasma Sci.*, vol. 43, no. 5, pp. 1198–1202, May 2015, doi: 10.1109/TPS.2015.2404439.

[39] J. Hagedorn, F. S. L. Blanc, and J. Fleischer, *Handbook of Coil Winding*. Berlin, Germany: Springer, 2018. [Online]. Available: https://link.springer.com/book/10.1007/978-3-662-54402-0#affiliations

[40] W. Chen et al., "Measurement of heating coil temperature for e-cigarettes with a 'top-coil' clearomizer," *PLoS ONE*, vol. 13, no. 4, Apr. 2018, Art. no. e0195925, doi: 10.1371/journal.pone.0195925.

[41] B. Kvasnica and P. Fabo, "Highly precise non-contact instrumentation for magnetic measurement of mechanical stress in low-carbon steel wires," *Meas. Sci. Technol.*, vol. 7, no. 5, pp. 763–767, May 1996, doi: 10.1088/0957-0233/7/5/007.

[42] M. L. Wang, D. Satpathi, S. Koontz, A. Jarosevic, and M. Chandoga, "Monitoring of cable forces using magneto-elastic sensors," in *Computational Mechanics in Structural Engineering*. Amsterdam, The Netherlands: Elsevier, 1999, pp. 337–347. [Online]. Available: https://www.sciencedirect.com/science/article/abs/pii/B9780080430089500648?via%3Dihub, doi: 10.1016/B978-008043008-9/50064-8.

Dongyoung Ko received the B.S. degree from the Department of Civil Engineering, Seoul National University of Science and Technology, Seoul, South Korea, in 2021. He is currently pursuing the M.S. degree from the Department of Global Smart City, Sungkyunkwan University, Suwon, South Korea.

His research interest includes the development of damage detecting technique by using elasto-magnetic (EM) sensor and finite elements method (FEM) simulation-based electromagnetic sensor optimization.

Jooyoung Park received the B.S. degree from the Department of Civil and Environmental Engineering, Sungkyunkwan University, Suwon, South Korea, in 2011, and the M.S. degree from the Department of Civil and Environmental System Engineering, Sungkyunkwan University, in 2014, where he is currently pursuing the Ph.D. degree.

His research interests include EM-based tension estimation of prestressed members and FEM simulation.

Junkyeong Kim received the B.S. degree from the Department of Polymer System Engineering, Sungkyunkwan University, Suwon, South Korea, in 2010, and the M.S. and Ph.D. degrees from the Department of u-City Design and Engineering and Department of Civil and Environmental System Engineering, Sungkyunkwan University, in 2012 and 2018, respectively.

He has been a Senior Research Engineer in the Technology Planning Team at the Advanced Institute of Convergence Technology, Suwon. His research interests include tensile force monitoring techniques for the prestressed tendons of PSC bridge girders using embedded EM sensors and machine learning methods.

Changjun Lee received the B.S. degree from the Department of Civil Engineering, Seoul National University of Science and Technology, Seoul, South Korea, in 2022, where he is currently pursuing the M.S. degree in global smart cities.

His research interests include light detection and ranging (LIDAR)-based structural safety monitoring for drones.

Hyungchul Yoon received the Ph.D. degree from the University of Illinois, Urban, IL, USA, in 2016.

He worked as an Assistant Professor at the Department of Civil and Environmental Engineering, Michigan Tech, MI, USA, from 2017 to 2018. He has been an Associate Professor at Chungbuk National University, Cheongju, Republic of Korea, since 2018. His research interests include vision-based structural health monitoring.

Seunghee Park received the Ph.D. degree from the Korea Advanced Institute of Science and Technology (KAIST), Daejeon, South Korea, in 2008.

He worked as a Postdoctoral Researcher at KAIST, from February 2008 to September 2008. He also worked as a Postdoctoral Research Fellow with the Center of Intelligent Material Systems and Structures, Department of Mechanical Engineering, Virginia Tech, VA, USA, from October 2008 to February 2009, where he was a Visiting Professor, from July 2009 to August 2009. He has been a Professor with Sungkyunkwan University, Suwon, South Korea, since March 2009.